Available online at www.sciencedirect.com

SCIENCE DIRECT®

Acta Materialia 53 (2005) 5033–5050

Acta MATERIALIA

www.actamat-journals.com

Whisker and Hillock formation on Sn, Sn–Cu and Sn–Pb electrodeposits

W.J. Boettinger *, C.E. Johnson, L.A. Bendersky, K.-W. Moon,
M.E. Williams, G.R. Stafford

Materials Science and Engineering Laboratory, Metallurgy Division, NIST, Mailstop 8555, 100 Bureau Dr., Gaithersburg, MD 20899, United States

Received 3 March 2005; received in revised form 20 July 2005; accepted 20 July 2005
Available online 8 September 2005

Abstract

High purity bright Sn, Sn–Cu and Sn–Pb layers, 3, 7 and 16 μm thick were electrodeposited on phosphor bronze cantilever beams in a rotating disk apparatus. Beam deflection measurements within 15 min of plating proved that all electrodeposits had in-plane compressive stress. In several days, the surfaces of the Sn–Cu deposits, which have the highest compressive stress, develop 50 μm contorted hillocks and 200 μm whiskers, pure Sn deposits develop 20 μm compact conical hillocks, and Sn–Pb deposits, which have the lowest compressive stress, remain unchanged. The differences between the initial compressive stresses for each alloy and pure Sn is due to the rapid precipitation of Cu_6Sn_5 or Pb particles, respectively, within supersaturated Sn grains produced by electrodeposition. Over longer time, analysis of beam deflection measurements indicates that the compressive stress is augmented by the formation of Cu_6Sn_5 on the bronze/Sn interface, while creep of the electrodeposit tends to decrease the compressive stress. Uniform creep occurs for Sn–Pb because it has an equi-axed grain structure. Localized creep in the form of hillocks and whiskers occurs for Sn and Sn–Cu because both have columnar structures. Compact hillocks form for the Sn deposits because the columnar grain boundaries are mobile. Contorted hillocks and whiskers form for the Sn–Cu deposits because the columnar grain boundary motion is impeded.
Published by Elsevier Ltd on behalf of Acta Materialia Inc.

Keywords: Whiskers; Electroplating; Creep; Grain boundary diffusion; Solder

1. Introduction

Sn whiskers have been an industrial concern and an interesting problem for many years. They are known to cause short circuits in fine pitch pretinned electrical components. In contrast to many whisker growth processes, Sn whiskers grow by the addition of material at their base not at their tip; i.e., they grow out of the substrate [1]. They can grow from as-formed electrodeposits, vapor deposited material [2] and intentionally deformed coatings of Sn [3]. Similar whiskers are observed in Cd, In and Zn. Whiskers appear to be a local response to the existence of residual stress and compressive residual stress is usually considered a precondition for whisker growth [3]. Annealing or melting (reflow in solder terminology) usually mitigates the growth, although subsequent bending of leads can re-establish compressive stress. In 1966, Pb additions of a few percent to Sn electroplate were found to greatly reduce the tendency to form whiskers [4] and interest in the subject waned. Recently, interest in Pb-free surface finishes for green manufacturing of electronic components has reopened this dormant field and an annotated bibliography has been prepared [5]. Questions remain as to the dominant source of stress and the precise growth mechanism. The final goal is the development of a practical mitigation strategy for electronic components during electroplating, storage and/or service.

---

* Corresponding author. Tel.: +1 301 975 6160; fax: +1 301 975 4553.
E-mail addresses: william.boettinger@nist.gov, wboettinger@nist.gov (W.J. Boettinger).

1359-6454/$30.00 Published by Elsevier Ltd on behalf of Acta Materialia Inc.
doi:10.1016/j.actamat.2005.07.016

As with Sn whiskers, compressive residual stress also plays a role in hillock growth on the surface of thin metal films made by vapor deposition. Hillock growth is often treated as a localized diffusional creep/grain boundary sliding phenomenon that relieves the compressive stress (see, for example [6–8]). The compressive stress is typically generated by the differential thermal contraction of the deposit and substrate during cooling from deposition temperature. On the other hand Sn electroplating is performed at room temperature; thus, residual stresses cannot have a thermal origin. One of the most commonly discussed sources of compressive stress in Sn electrodeposits is intermetallic compound (IMC) formation due to the reaction of Sn with Cu in the substrate metal [9–11]. Despite the differences between hillock growth on vapor deposited metals and Sn whisker growth from electrodeposits, localized creep is a potential mechanism for both.

In a previous paper [12], it was shown that filamentary whisker defects were not observed on bright pure Sn electrodeposits if high purity (18 MΩ cm) water was used to prepare the commercial methanesulfonate electrolyte. Intentional Cu additions as an impurity to the electrolyte in the range from 0.5×10^{-3} to 25×10^{-3} mol/L did however cause whiskers and hillocks to form. But IMC forms on the interface between the deposit and the substrate for both pure Sn and Sn–Cu deposits. Thus, we questioned whether IMC formation on the interface between the substrate and the deposit was the major stress source for whisker formation, especially because electroplating itself often produces significant residual stress in deposits [13].

Using deflection measurements of plated cantilever beams, the present paper seeks to determine whether the in-plane residual stress in Sn–Cu electrodeposits is compressive and greater than that for pure Sn electrodeposits. Sn–Pb alloys were included in the study because of the known whisker mitigation effect of Pb. The paper also determines the relative amounts of stress generated by the electrodeposition process, the alloy additions and how the reaction at the deposit/substrate boundary changes the deposit stress with time. The paper reports the propensity for whisker/hillock formation and the interior microstructure of the electrodeposits and compares this tendency with the stress and plastic strain rate of the deposits. Finally, a mechanism based on localized creep of columnar grain structures is suggested for the localized surface disturbance in response to the compressive stress.

2. Reaction of Sn with Cu

The formation of the layer of Cu_6Sn_5 by reaction between Cu and a layer of Sn is a relatively slow process controlled by diffusion. Onishi and Fujibuchi [14] measured the intermetallic growth rates in diffusion couples between Cu and Sn between 109 and 220 °C. The thickness of the total intermetallic layer ($Cu_6Sn_5 + Cu_3Sn$) is given by

$$d_{\mathrm{IMC}} = \sqrt{Bt} \tag{1}$$

with $B = 6.23 \times 10^{-6} \exp(Q/RT)$ cm^2/s and $Q = 57.7$ kJ/mol. At 298 K, the extrapolated value of B is 4.7×10^{-16} cm^2/s. A square root of time dependence is valid as long as the intermetallic layer is much thinner than the Sn and Cu layers. Alternately, Tu and Thompson [15] have measured the growth rate of intermetallic at room temperature. They observed only Cu_6Sn_5 and obtained

$$d_{\mathrm{IMC}} = B't \tag{2}$$

with $B' = 4 \times 10^{-12}$ cm/s for IMC thicknesses up to 300 nm. This linear form implies that interface attachment kinetics is dominant for room temperature IMC growth, not diffusion, at least in its initial stage. Finally, in unpublished work [16] using Sn plating on a Cu metallized quartz crystal resonator and electrochemical stripping after different hold times, the intermetallic was found to grow as $\sqrt{Bt}$ at room temperature with $B = 1.76 \times 10^{-15}$ cm^2/s. Below, we present measurements of residual stress in deposits 15 min after plating. The above considerations indicate that less than 20 nm of intermetallic can form during this time and would have negligible effect on the stress in 3–16 μm thick deposits. On the other hand, the above suggests that between 1.2 and 2.3 μm may form in a year (3×10^7 s) and the stress of the deposit may be influenced at longer times.

For pure Sn in contact with a Cu substrate, we do not expect, nor has it ever been observed to our knowledge, that discrete (isolated) intermetallic particles form on Sn grain boundaries due to rapid diffusion of Cu from the substrate. The supersaturation required to nucleate a discrete IMC particle could only occur during the short period of time before a continuous layer of the same IMC coats the Cu/Sn interface. After that time, formation and/or further growth of discrete IMC particles on grain boundaries is not possible. Similarly, we have not observed rapid penetration of IMC along Sn grain boundaries. However, as shown below, when Cu^{2+} is present in the electrolyte, discrete IMC particles can form within the Sn grains and along grain boundaries by solid state precipitation from a Cu supersaturated Sn solid solution formed by electrochemical co-deposition. The distinction is important because, as argued below, the stress-free strains caused by the two processes differ in sign.

3. Experimental method

Using a metal shear, coupons, 2.5 cm square, were cut from 152 μm thick, half hard, rolled phosphor bronze with nominal mass fractions of Cu–5%Sn–(0.03–0.35)%P. The edges were deburred with a jeweler's file and the surface to be plated was polished with 0.3 μm Al_2O_3. Using the geometry shown in Fig. 1, cantilever beams, 2 mm × 20 mm, and a supporting frame were chemically etched from the coupons using acid resistant tape and 60% nitric acid. It was found necessary to employ beams perpendicular to the sheet rolling direction to obtain reproducible beam deflections after plating. This may lead to a non-isotropic biaxial response of the beams, but this factor will be ignored.

Prior to electroplating, all substrates were immersed in 25% sulfuric acid solution for 5 s to remove oxide and were rinsed in deionized water. Bright electrodeposits of Sn, Sn–Cu and Sn–Pb alloys were electrodeposited from a commercial methanesulfonate electrolyte containing 340 mmol/L Sn^{2+}. The electrolyte was prepared with high purity water with a resistivity of 18.3 MΩ cm. The cantilever samples were attached with plater's tape to a disk electrode assembly and rotated during plating at 100 rotations per min to provide reproducible hydrodynamic conditions. This rotation speed creates a uniform hydrodynamic boundary layer approximately 40 μm thick along the electrode surface [17]. All coupon surfaces except the cantilever were masked. Plating was performed at a constant current density of 60 mA/cm^2 in 1 L of solution at 25 ± 0.5 °C to various average thicknesses between 3 and 16 μm (determined by weight gain after plating). The anode was a 99.999% pure Sn sheet. The plating efficiency was between 98% and 100%. Thus, hydrogen evolution is not thought to affect the results of this study. The coupons were removed from the bath while still electrified. At this current density, the plating rate is approximately 0.05 μm/s and 320 s is required to form a 16 μm deposit. For the Sn–Cu deposits the Cu^{2+} concentration in the electrolyte was 15.0 mmol/L by the addition of copper methanesulfonate [$Cu(CH_3SO_3)_2$]. An examination of the alloy-electrolyte compositions reported in [12] indicates that the co-deposition of copper is diffusion-limited at this Cu^{2+} concentration and current density. For the Sn–Pb deposits the Pb^{2+} concentration in the electrolyte was 9.2 mmol/L by the addition of lead methanesulfonate [$Pb(CH_3SO_3)_2$].

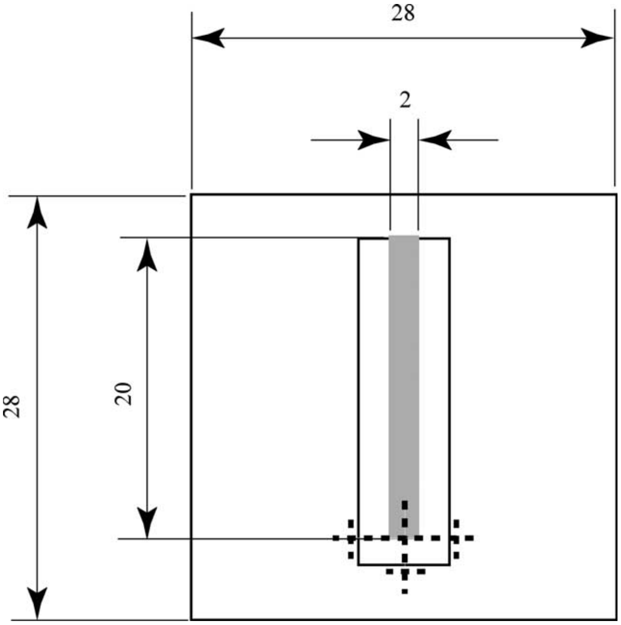

Fig. 1. Drawing of a cantilever beam coupon with plated region shown in gray. The three frame positions used for tip position measurement are indicated. Dimensions are in mm.

After electrodeposition, the plating tape was dissolved with acetone and the samples were rinsed with deionized water. For each coupon, the position of the beam tip with respect to the frame was measured before plating, within 15 min after plating and then at various times up to 2×10^6 s (20 days). The height of the beam tip with respect to the frame was measured at three positions as shown in Fig. 1 by the changes in focus position in an optical microscope. These measurements were done with the coupon horizontal in the two orientations with respect to gravity. Correction was made for the increased thickness of the beam due to plating. The position of the beam at each time was taken as the mean of the six measurements. The change in position from the initial position (prior to plating) is defined as the deflection. A negative deflection means that the electrodeposit surface is convex indicating that the deposit wants to expand (positive stress-free strain), the constraint of the underlying substrate putting the deposit in biaxial in-plane compression.

The plated surfaces were examined without preparation for the presence of whiskers and/or hillocks using optical and scanning electron microscopy (SEM). Selected samples were prepared for optical and SEM metallographic cross-sectional examination by mounting in epoxy and using standard polishing procedures. Sn, Sn–Cu and Sn–Pb samples plated on amorphous carbon were prepared for chemical analysis and for transmission electron microcopy (TEM) by cold stage precision ion milling.

Tensile tests with strain gauges were conducted on the 150 μm thick phosphor bronze substrate material. Young's modulus and Poisson's ratio were determined to be 134 ± 1.6 GPa and 0.386 ± 0.02, respectively. Microhardness measurements were performed on cross-sections of the 16 μm thick electrodeposits. A Knoop indenter with 1 g load was employed and oriented with the long axis parallel to the plating surface. Using the approximation that the yield stress is 1/3 of the microhardness, yield strength values of 44 ± 2, 64 ± 4 and 44 ± 4 MPa were obtained for the pure Sn, Sn–Cu and Sn–Pb deposits, respectively. The higher yield stress of the Cu–Sn deposits is likely due to the presence of the hard intermetallic particles. All measured stresses in the deposits are below these yield stress values.

4. Results

4.1. Surface microstructure of deposits

On pure Sn deposits, compact conical hillocks approximately 2 μm high × 2 μm wide appear within 900 s of plating. These appear to be grains that have risen from the surface. Within two days, approximately 10% of the small hillocks grow while the others remain the same size. This process produces the bimodal surface structure shown in Fig. 2. Grain boundary groves are also apparent on the deposit surface. Multiple electron backscatter diffraction patterns taken from the small and large conical hillocks show most to be single grains. Patterns taken from 26 conical hillocks surface showed no obvious preferred orientation. The single grain structure of the conical hillocks was confirmed by an SEM image of a focused ion beam (FIB) cross-section (Fig. 3) on a 16 μm thick Sn sample [18]. We note a significant change in the as-plated columnar grain structure of the deposit under the hillock. Significant grain boundary motion has occurred in conjunction with the development of the hillock. It is important to note that the continuous white contrast on the Sn columnar grain boundaries is not IMC formed by diffusion up the grain boundaries. It is an artifact of the FIB procedure (see Fig. 9) as is the darker contrast in the hillock grain above the deposit surface.

Filamentary whiskers and hillocks were evident on the Sn–Cu deposits within 2 days of plating. Fig. 4 shows SEM views of a 16 μm thick Sn–Cu alloy deposit surface. The hillocks are not conical and have a contorted appearance. They are also much larger (50 μm wide × 50 μm wide) than the conical hillocks in the pure Sn deposits. Whiskers appear to spew forth from approximately 10% of these features. However, the whiskers actually appear first followed by continued accumulation of Sn at the base. The grain boundaries on the undisturbed part of the surface are difficult to identify because of a fine dispersion of particles and have been sketched in. These particles are Cu_6Sn_5 that have coarsened over several months from the initially fine precipitates seen by TEM that formed within the Sn grains shortly after plating (as described below). To obtain a sense of the time scale during which the surface disturbances grow, Fig. 5 shows a sequence of SEM photographs of a feature that grew in volume with time. Contorted hillocks and whisker filaments occur on the same sample (Fig. 4). Both are shown in Fig. 6, which are SEM images of FIB cross-sections [18] at two positions on a single 16 μm thick Sn–Cu sample. Note that the as-plated grains are columnar. The contorted hillock shape forms because of the activity of more than one grain under the disturbance and the IMC hindered grain boundary motion under the hillock. Grain boundary pinning appears to have been very effective under the filamentary whisker where no grain boundary motion has occurred in the deposit under the filament.

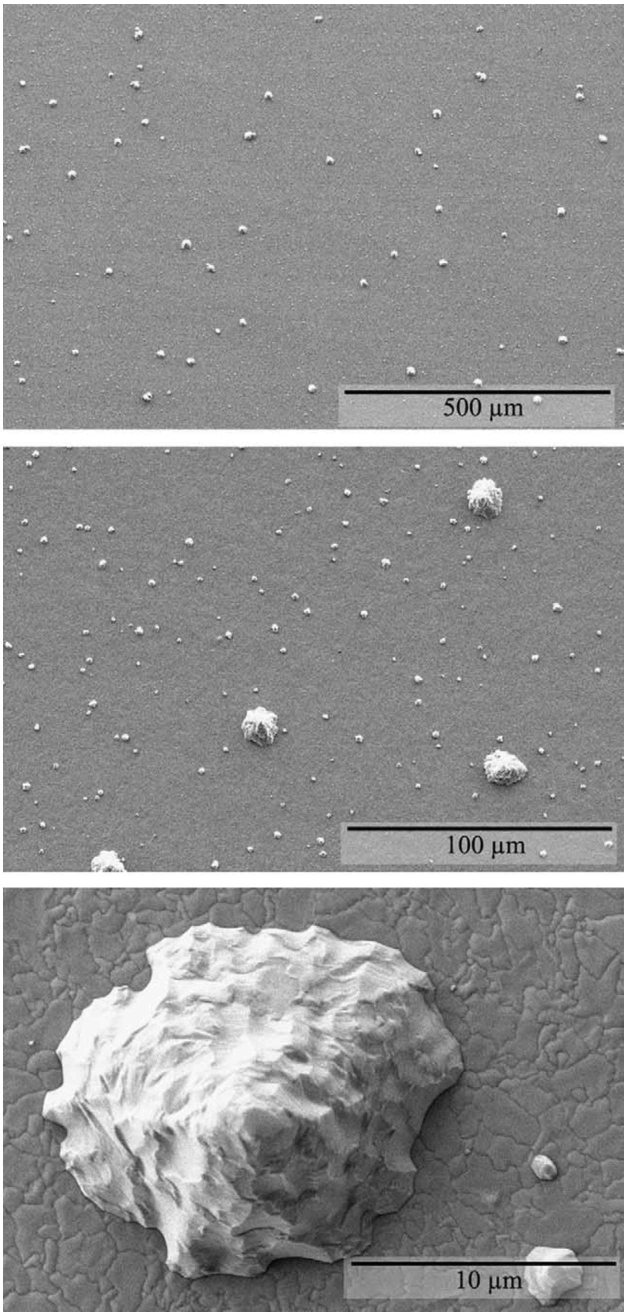

Fig. 2. Low, intermediate and high magnification SEM micrographs of the electrodeposit surface of a 16 μm thick pure Sn electrodeposit on a cantilever beam showing bimodal size distribution of conical hillocks.

Fig. 7 shows SEM views of a 16 μm thick Sn–Pb electrodeposit surface 85 days after plating. The surface is free of hillocks and whiskers. Only grain boundary grooves are evident. The backscattered SEM image shows that coarsened Pb particles exist as separate grains mixed with Sn grains. A FIB cross-section (Fig. 8) [18] shows that the grain structure of the Sn–Pb electrodeposit is *not* columnar. Compared to the Sn

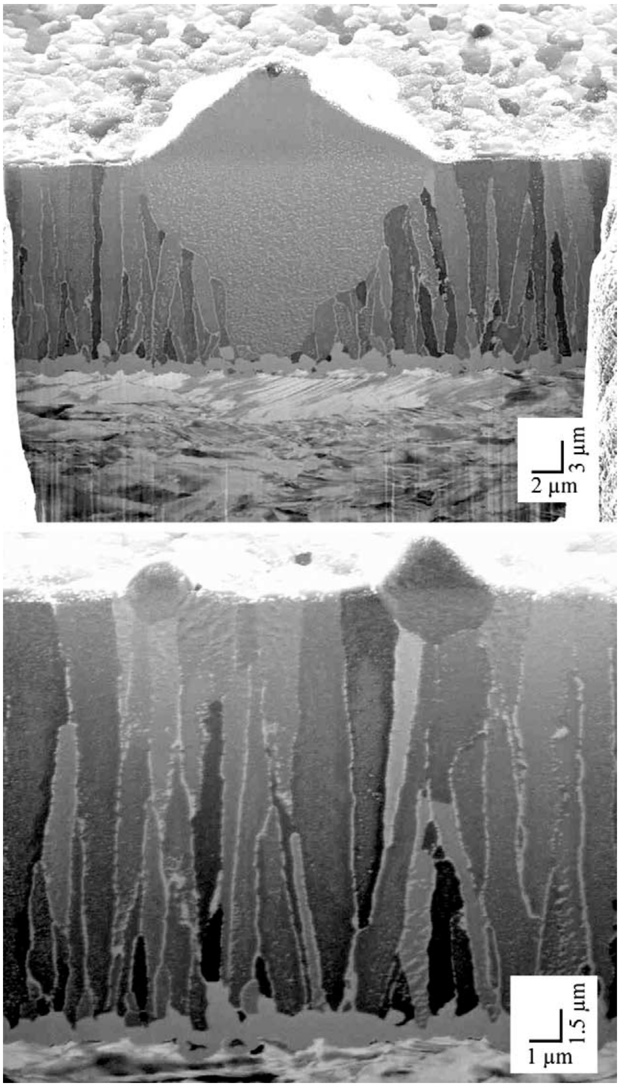

Fig. 3. SEM image of FIBed sample showing small and large hillocks on a 16 μm thick pure Sn electrodeposit. IMC and the bronze are seen at the bottom [18]. The white contrast on the Sn columnar grain boundaries is an artifact of the FIB procedure as is the darker contrast in the hillock grain above the deposit surface.

and Sn–Cu deposits, the Sn–Pb deposits have many more grain boundaries parallel to the top surface. It is known that the co-deposition of Pb significantly reduces any crystallographic texture in the Sn by preventing columnar growth [19].

Examination of the surfaces of the various 3 and 7 μm thick deposits showed the same structures noted above. However, after cantilever measurements were stopped, re-examination of the surfaces after 2.5 years showed that while the 7 and 16 μm thick deposits surfaces remained the same, the 3 μm thick Sn deposit had developed a very low density of conical hillocks and long filamentary whiskers and the 3 μm thick deposit of Sn–Pb had developed a low density of short 20 μm long whiskers. It is possible that excessive handling of the cantilevers led to these changes for the thin deposits.

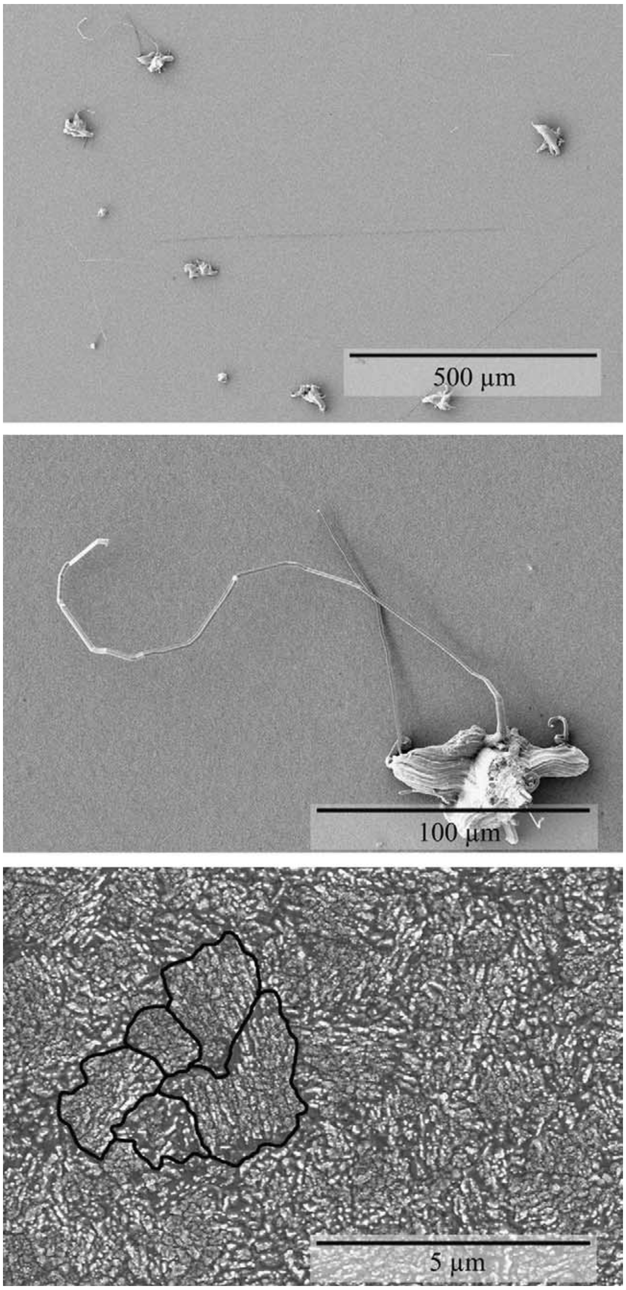

Fig. 4. Low, intermediate and high magnification SEM micrographs of the electrodeposit surface of a 16 μm thick Sn–Cu electrodeposit on a cantilever beam (photo taken after 176 days (1.5×10^7 s)). The fine lines center and lower right in the top figure are long whiskers. A few Sn grain boundary locations are indicated in the bottom figure.

4.2. Internal deposit microstructure, composition and microhardness

SEM micrographs of metallographic cross-sections of the 16 μm (average) deposits of the three alloys are shown in Fig. 9. The columnar grain structure of the Sn and Sn–Cu deposits is confirmed. These samples were approximately one-year-old (3×10^7 s) when sectioned.

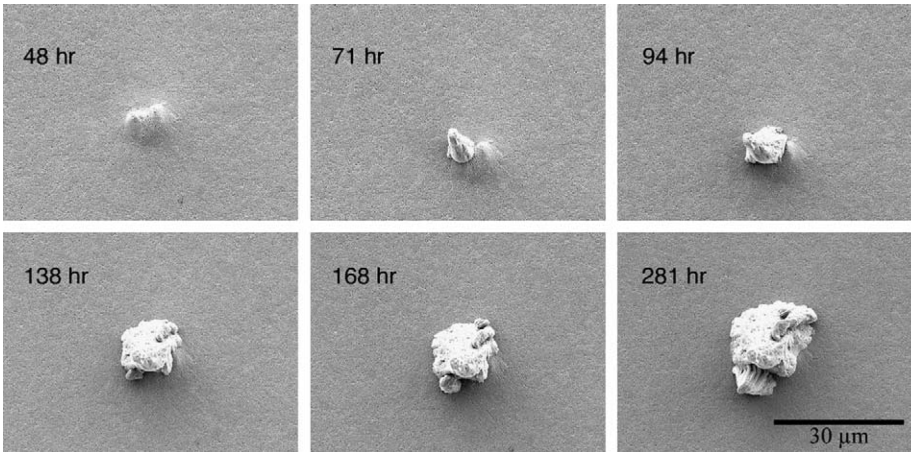

Fig. 5. Time sequence of the formation of an eruption on a Sn–Cu 16 μm thick cantilever sample. Prior to 2 days (1.5×10^5 s) no surface upheaval is observed.

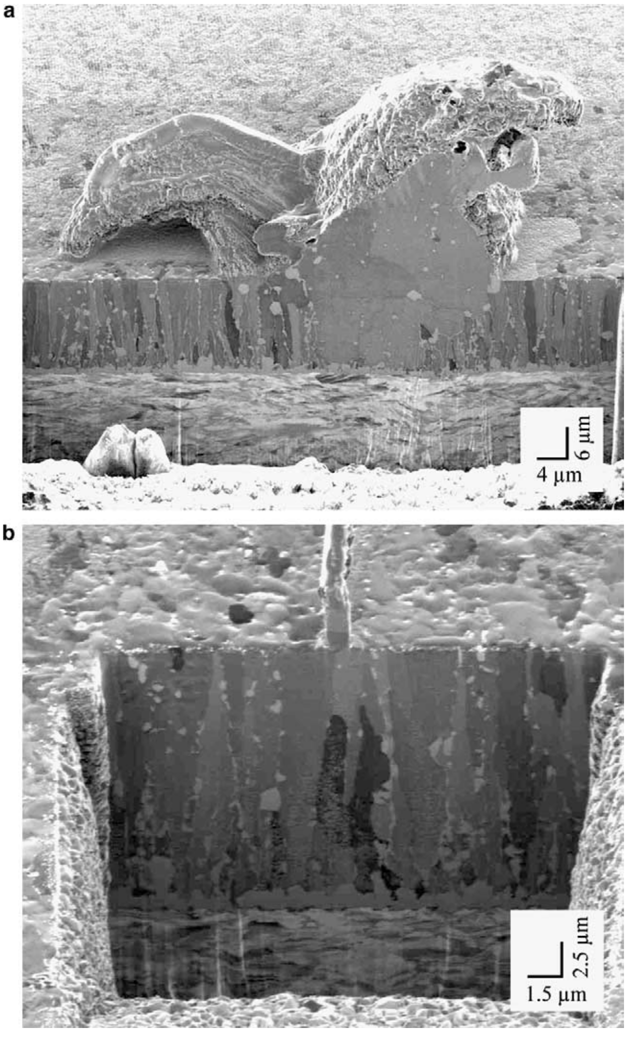

Fig. 6. SEM images of FIBed 16 μm thick Sn–Cu electrodeposit: (a) location showing a contorted eruption; (b) location showing a filamentary whisker on the same sample [18].

In all three micrographs, a 1.5–2.5 μm thick scalloped intermetallic Cu_6Sn_5 layer is seen on the interface between the deposit and the substrate. A much thinner Cu_3Sn layer is also present but not visible. The thickness of the Cu_6Sn_5 layer is in general agreement with that described in Section 1. In the Sn–Cu deposits intermetallic Cu_6Sn_5 is also seen distributed throughout the deposit, primarily on Sn grain boundaries. No IMC is seen on the grain boundaries of the pure Sn or Sn–Pb samples. We again note the presence of many transverse grain boundaries in the Sn–Pb deposit compared to the pure Sn and Sn–Cu deposits. The Pb phase location is not revealed in these micrographs.

Determining the deposit over-all composition proved difficult due to the low solute levels, small sample volumes and the two-phase nature of the deposits. Several methods were used: inductively coupled plasma spectrometry analysis (ICP), energy dispersive spectroscopy (EDS) in the SEM from area scans (10 μm in the plating direction by 20 μm) of cross-sectioned 16 μm thick deposits, and the area fraction of Cu_6Sn_5 (excluding that on the bronze/Sn interface) for the Sn–Cu deposit. The Cu concentration ranged between 1.4% and 3.7% mass fraction Cu depending on the method used. The area fraction of Pb in the Sn–Pb sample could not be measured due to polishing difficulties. The other measurement methods gave Pb concentrations between 1.0% and 3.5% mass fraction Pb. Because the deposition conditions were tightly controlled, we do not believe these ranges represents true variation in sample composition. The expected Cu concentration, based on diffusion-limited Cu^{2+} and a diffusion coefficient of 5×10^{-6} cm^2/s [20], is 3.3% mass fraction Cu. We will set the compositions to be 3% mass fraction Cu and 2% mass fraction Pb for the analysis below.

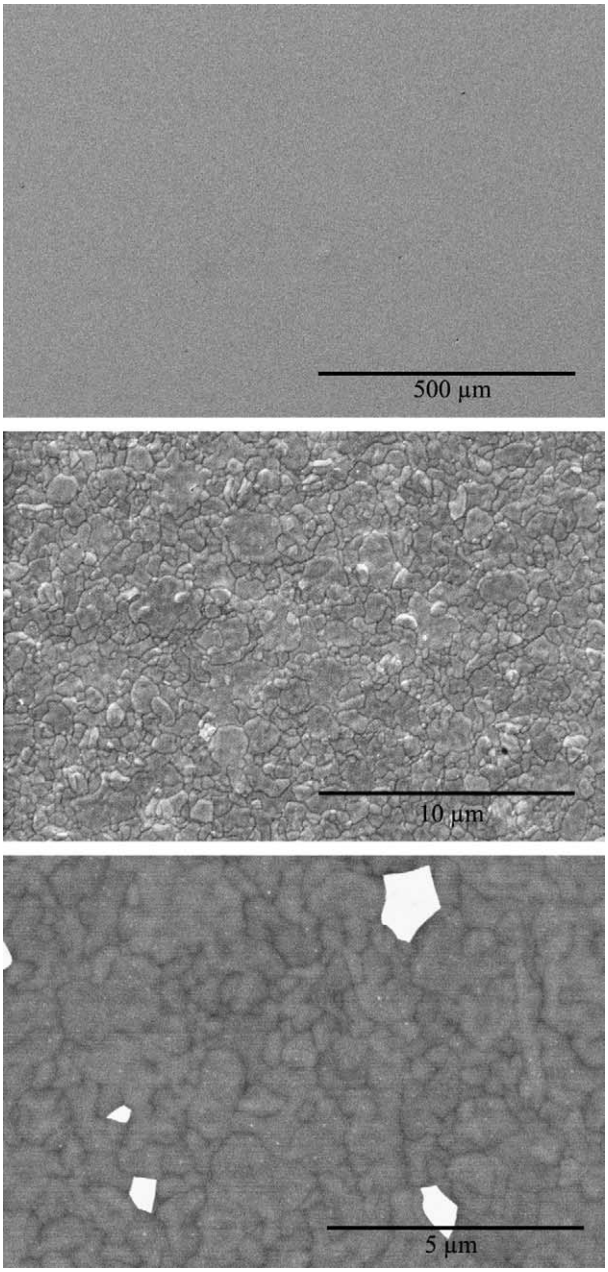

Fig. 7. Low, medium and high magnification SEM micrographs of the electrodeposit surface of a 16 µm thick Sn–Pb electrodeposit on a cantilever beam after 85 days (7.3×10^6 s). The highest magnification SEM micrograph employed back scattered electron contrast and clearly shows four isolated Pb grains.

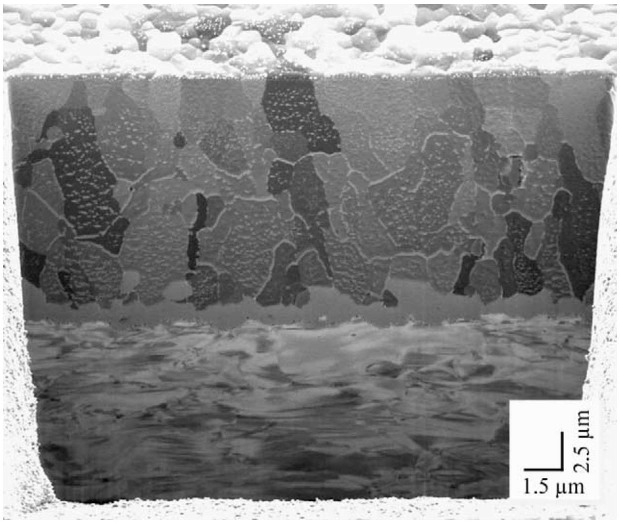

Fig. 8. SEM images of FIBed 16 µm thick Sn–Pb electrodeposit. The grain structure is not columnar [18].

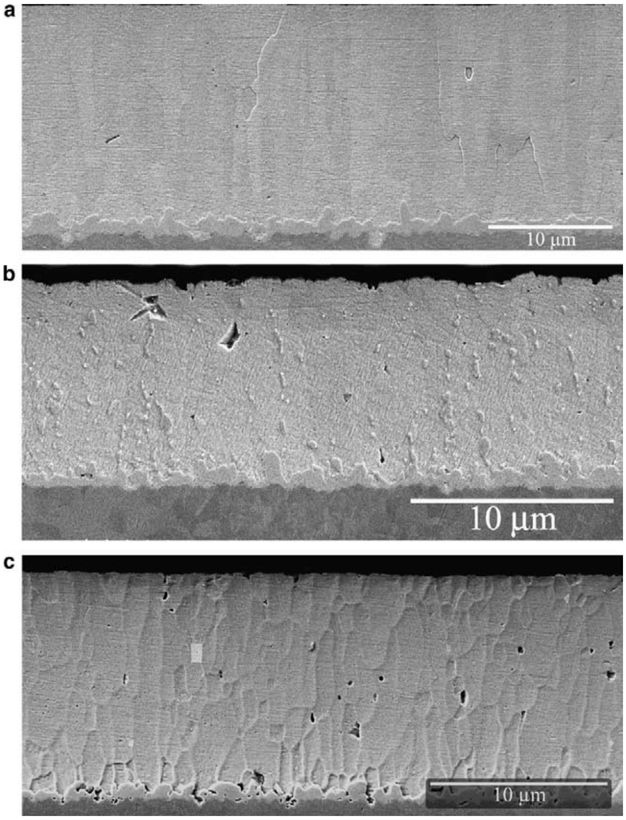

Fig. 9. Cross-sections of 16 µm thick (nominal) electrodeposits on phosphor bronze: (a) pure Sn; (b) Sn–Cu; (c) Sn–Pb approximately one year after plating.

TEM examination (Fig. 10) of a Cu-containing deposit on glassy carbon one day after deposition shows fine intermetallic precipitates within the Sn grains and a few on the grain boundaries. It is well known that electrodeposition is capable of producing alloy deposits that are super-saturated; i.e., they contain more alloying addition than the phase diagram permits at the temperature of deposition [21]. It is likely that the fine IMC particles in Fig. 10 form by precipitation from solid solution quite rapidly after plating (within 10^3 s) and evidently coarsen over several months when they appear mostly along the Sn grain boundary as seen in Fig. 9. Similarly, Sheng et al. [22] found many grain boundary

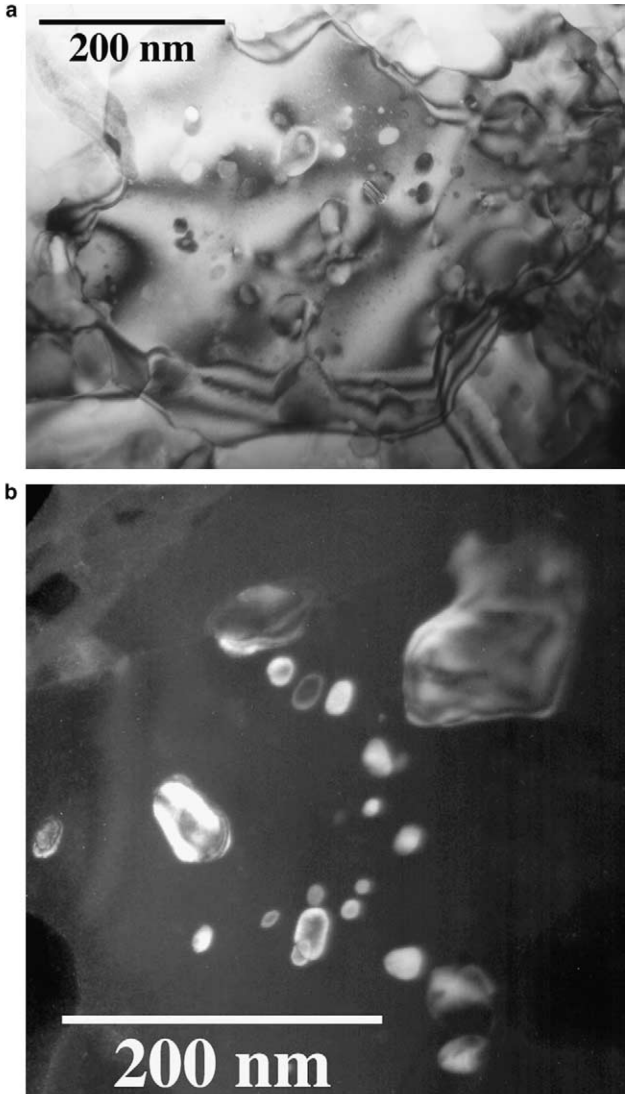

Fig. 10. TEM (a) bright and (b) dark field views of Sn–Cu deposit approximately 24 h after electroplating. Cu_6Sn_5 intermetallic particles were identified by SAD in the interior of the Sn grains and on the grain boundaries. The dark field images show that the internal particles share a common orientation.

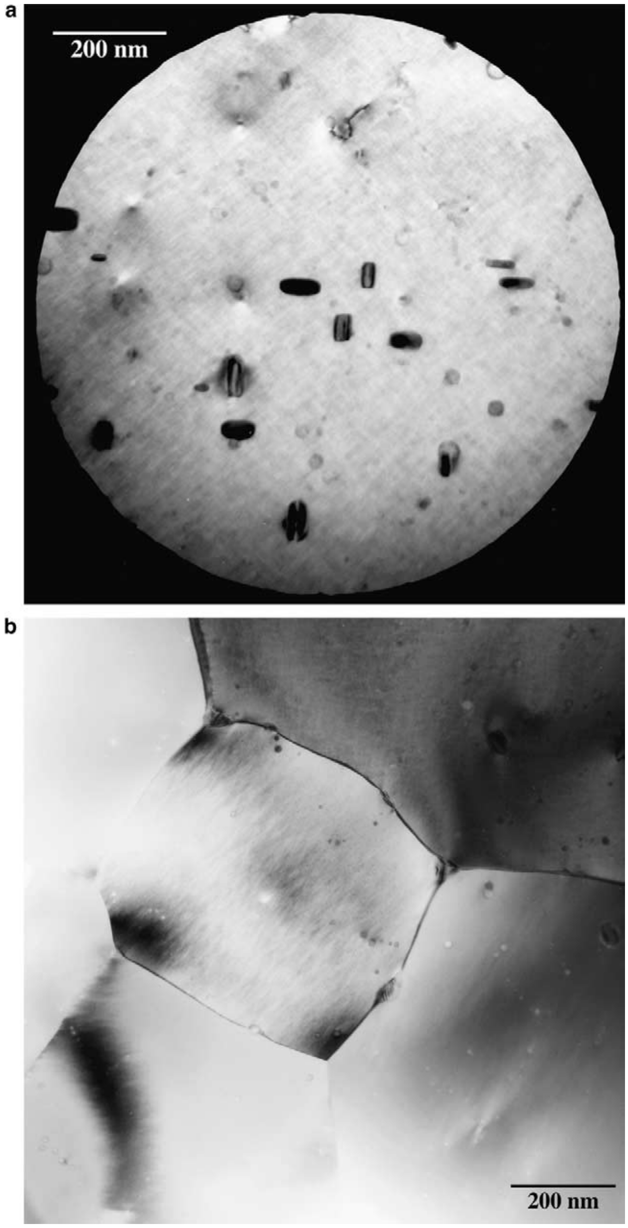

Fig. 11. TEM of Sn–Pb electrodeposit one month after plating: (a) Pb particles are approximately 50 nm tetragonally distorted cuboids within the Sn grains and (b) larger Pb particles on the Sn grain boundaries.

precipitates of Cu_6Sn_5 in aged Sn–Cu electrodeposits of eutectic composition on Cu leadframes but very few in samples with a pure Sn finish. We note that supersaturation of Sn with up to 2.2% mass fraction Cu has been reported using rapid solidification and immediate diffraction measurements at liquid nitrogen temperature [23]. Thus, similar supersaturation by electrodeposition is likely.

TEM examination of a Pb-containing sample one day after deposition on glassy carbon showed extremely fine (10 nm) spherical precipitates of Pb. One month after plating (Fig. 11), the Pb particles are approximately 50 nm tetragonally distorted cuboids within the grains and larger particles on the Sn grain boundaries. Table 1 summarizes the observed surface defects and the internal microstructures of the deposits.

4.3. Hillock volume

Measuring the total amount of material pushed up above the deposit surface during whisker growth is difficult due to the irregularity of the shapes. The regularity of the conical hillocks observed on the 16 μm thick pure Sn electrodeposits provides an opportunity for such a measurement. The distribution of projected areas (onto the plated surface) of the hillock population was measured

Table 1
Summary of surface defects and microstructure of the deposits

	Sn	Sn–Cu	Sn–Pb
Surface defects	Conical hillocks	Contorted hillocks and filamentary whiskers	None
Sn grain structure	Columnar, mobile	Columnar, immobile	Equi-axed
Initial alloy structure	–	Fine Cu_6Sn_5	Fine Pb
Aged alloy structure	–	Coarse Cu_6Sn_5 on grain boundaries	Sparse equi-axed Pb grains

Cu_6Sn_5 forms slowly on the deposit/substrate boundary for all.

by quantitative metallography 7.86×10^6 s after plating. Each hillock was assumed to be a cone with a radius derived from its measured projected area and with an apex semi-angle (estimated from FIB cross-sections) of 45° for the small hillocks and 58° for the large hillocks of the bimodal distribution. The total hillock volume per unit plated surface area is 0.012 μm. We estimate that about a third of this volume develops within 1 h of plating. Dividing by the deposit thickness, 16 μm, an average volumetric plastic strain, $\Delta V/V$, of 8×10^{-4} was determined. An estimate of the in-plane biaxial stress that was relieved by this hillock formation [24] is

$$\Delta\sigma = \frac{E'_f}{2}\frac{\Delta V}{V}, \tag{3}$$

where E'_f is the biaxial modulus of Sn (78 GPa, see Table 2). The compressive stress reduction is 30 MPa. This number is of the same order as, but about twice, the stress relaxation measured over the 7.86×10^6 s by the cantilever beam measurements.

4.4. Cantilever beam deflection measurements

4.4.1. Initial deflection

After release from the rotating assembly, the deposit side of all cantilever beams was immediately convex; i.e., the deflection is negative. This indicates that the deposit wants to expand with respect to the beam and is thus in a state of compressive stress due to the constraint of the substrate. First, we examine the average stress in the deposit determined from the earliest deflection measurement at approximately 10^3 s shown in Fig. 12. As described above, the intermetallic on the bronze/Sn interface is quite thin (20 nm) at this time and can be neglected. To treat the 16 μm thick electrodeposit, the first-order correction to Stoney's equation is required. We assume that the bi-axial in-plane stress in the deposit before it is released from the rotating disk is uniform. The stress before release to first order depends on the modulus of the deposit. However, the stress in the deposit after it is released, σ_f, does not depend on the modulus of the deposit and is given by

$$\sigma_f = \frac{E'_S}{6}\frac{d_S^2}{d_f}K\left[1 - \frac{d_f}{d_S}\right] = \frac{E'_S}{3}\frac{d_S^2}{d_f}\frac{\delta}{L^2}\left[1 - \frac{d_f}{d_S}\right], \tag{4}$$

where the notation is defined in Table 2. Brenner and Senderoff [25] summarize various approximations for thick deposits.

Table 2
Parameters for Stoney's equation and other mechanical parameters

E'_S = substrate biaxial modulus = $E_S/(1 - \nu_S)$ = 216 GPa (E_S = 134 GPa, ν_S = 0.386)
d_S = substrate thickness = 152 μm
d_f = film thickness = 3, 7, 16 μm
L = beam length = 20 mm
δ = deflection of beam from position prior to plating
K = curvature of beam = $2\delta/L^2$
E'_f = Sn biaxial modulus = 78 GPa (E_S = 50 GPa, ν_S = 0.357 [26])
E'_{IMC} = Cu_6Sn_5 biaxial modulus = 122 GPa (E_S = 86 GPa, ν_S = 0.3 [27])

Fig. 13 shows a plot of the initial compressive stress (approximately 15 min after plating) vs. deposit thickness for the three deposit compositions using the parameter values in Table 2. All stresses are compressive. For each alloy, the initial stress becomes more compressive with increasing thickness. Because the diffusion fields in the electrolyte, and thereby the deposit alloy compositions, reach steady-state within the first 0.1 μm of deposition due to the rotation of the electrode, the observed stress-thickness relationship cannot be attributed to a concentration gradient in the deposition direction. The reason for the increase in the magnitude of the compressive stress with deposit thickness is unclear.

Regardless of deposit thickness, the Sn–Cu deposits have the highest compressive stress, the pure Sn has intermediate compressive stress, and the Sn–Pb deposit has the lowest compressive stress. A positive correlation exists between the magnitude of the compressive stress and the degree of disruption of the surface morphology; viz., the Sn–Cu samples have whiskers and large contorted hillocks, the pure Sn has only small hillocks and the Sn–Pb alloys are free of hillocks and whiskers.

4.4.2. Deflection vs. time

As shown in Fig. 12, the beams return toward their initial positions with many of the samples actually passing through the initial position. Use of Eq. (4) would imply that the deposit stress begins compressive and becomes tensile with time. However this is not necessarily correct. To determine the average stress and the strain rate in the Sn and Sn alloy deposits from the

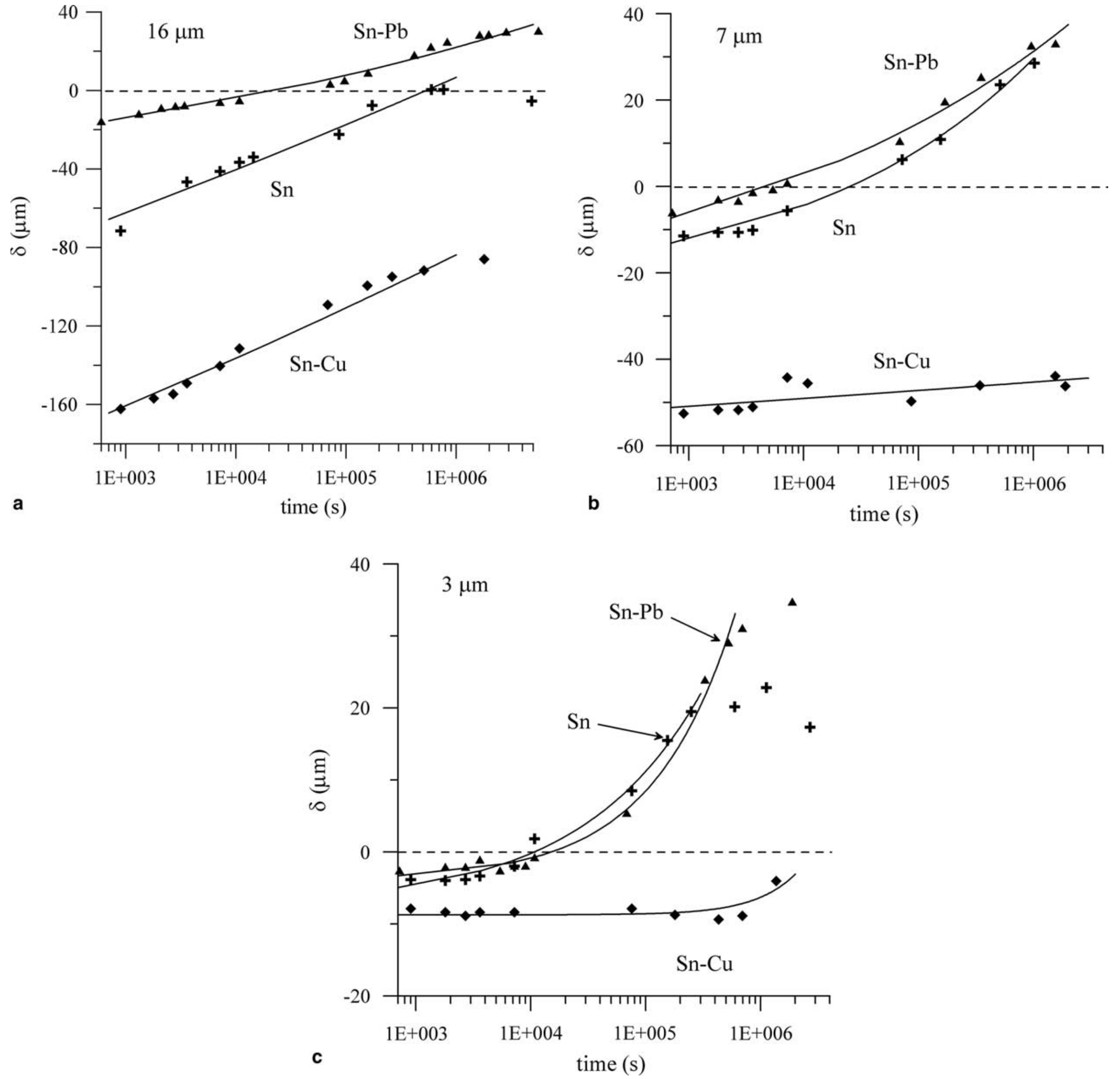

Fig. 12. (a) Deflection vs. time for 16 μm thick deposits. Lines are power law fits. (b) Deflection vs. time curves for 7 μm thick deposits. Lines are power law fits. (c) Deflection vs. time curves for 3 μm thick deposits. Lines are power law fits.

deflection data, we need to perform a "two layer Stoney analysis", one layer for the deposit and one for the growing IMC. The details of a model are given in the Appendix and the analysis of the time dependence will be deferred to the discussion.

5. Discussion

5.1. Molar volume of Sn–Cu and Sn–Pb alloys

Before we can analyze the reasons for the various states of stress in the deposit, it is necessary to consider the molar volume (volume per mole of atoms) for Sn–Cu and Sn–Pb alloys as summarized by Fig. 14. For Sn–Cu, crystallographic data was used for the pure elements and the Cu-rich phases. For Cu_6Sn_5, Fields et al. [27] measured a density of 8.28 g/cm^3 that converts to 10.6 cm^3/mol[1] (of atoms) using the composition of 0.44 atomic fraction Sn given in [28]. In the same manner, the measured density of Cu_3Sn, 8.90 g/cm^3, converts to 8.6 cm^3/mol. The equilibrium solubility of Cu in solid Sn is very small: 6×10^{-3} mass fraction Cu at 227 °C [29] and 10^{-7} mass fraction Cu at room temperature (thermodynamic calculation [30]). As noted above, however, there is evidence from Fig. 10 that a supersat-

---

[1] The measured density agrees with the measured lattice parameters of the $B8_2$ ($P6_3/mmc$) structure of Cu_6Sn_5 if one considers the vacant 2d Wycoff sites required to achieve the correct phase composition.

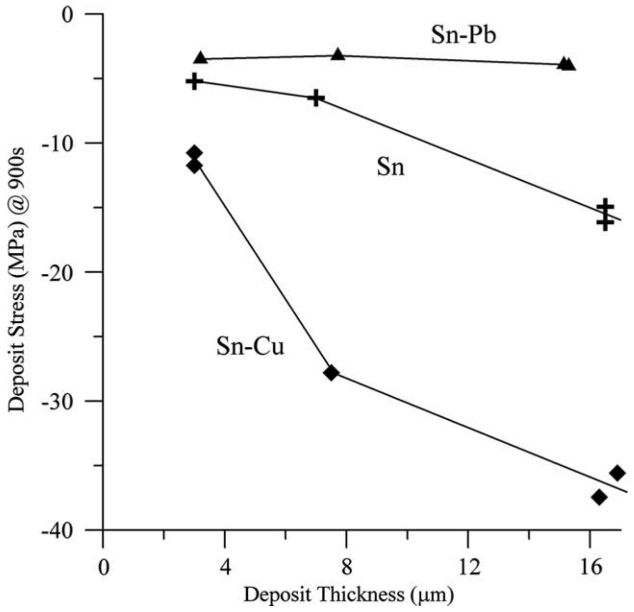

Fig. 13. Initial stress (approximately 15 min after plating) as a function of plating thickness.

urated solid solution of Cu in Sn is formed by the electrodeposition process. Because no lattice parameter data was reported in [23], we require an estimate of the molar volume of Sn supersaturated with Cu, Sn(Cu). Given the work on fast diffusion[2] of Cu in Sn, the presumption that the Cu is dissolved interstitially in Sn [31,32], and assuming that the partial molar volume of interstitial Cu is zero, the volume per mole of atoms of supersaturated Sn(Cu) is shown in Fig. 14 and is given by

$$V_{\mathrm{M}}^{\mathrm{Sn(Cu)}} = 16.28(1 - X_{\mathrm{Cu}}), \qquad (5)$$

where X_{Cu} it the mole fraction of Cu. These considerations would imply that the lattice parameter of Sn is unchanged by the interstitial Cu. The lattice parameters for the Sn–Pb system are summarized in Ref. [33]. Specifically, Sn rich Sn(Pb) solid solution up to 0.012 mass fraction Pb were measured at 183 °C in [34]. After conversion from kX units to SI units and changing the value of the intercept to get the accepted value for pure Sn at room temperature, the results are

$$V_{\mathrm{M}}^{\mathrm{Sn(Pb)}} = 16.28 + 3.52X_{\mathrm{Pb}}, \qquad (6)$$

where X_{Pb} it the mole fraction of Pb. This expression is plotted in Fig. 14.

We extract a few numbers from Fig. 14 for use below. First, the formation of a layer of Cu_6Sn_5 at an interface between Sn and Cu is considered. The volumetric strain for this process can be read directly from the graph or determined analytically. It is the difference between the molar volume of the Cu_6Sn_5 and the molar volume of an unalloyed mixture of pure Cu and pure Sn of the same average composition as the intermetallic. The fractional change is −0.056. In other words, the IMC takes up 5.6% less volume than a rule of mixture combination of the Sn and Cu reactants from which the IMC forms.

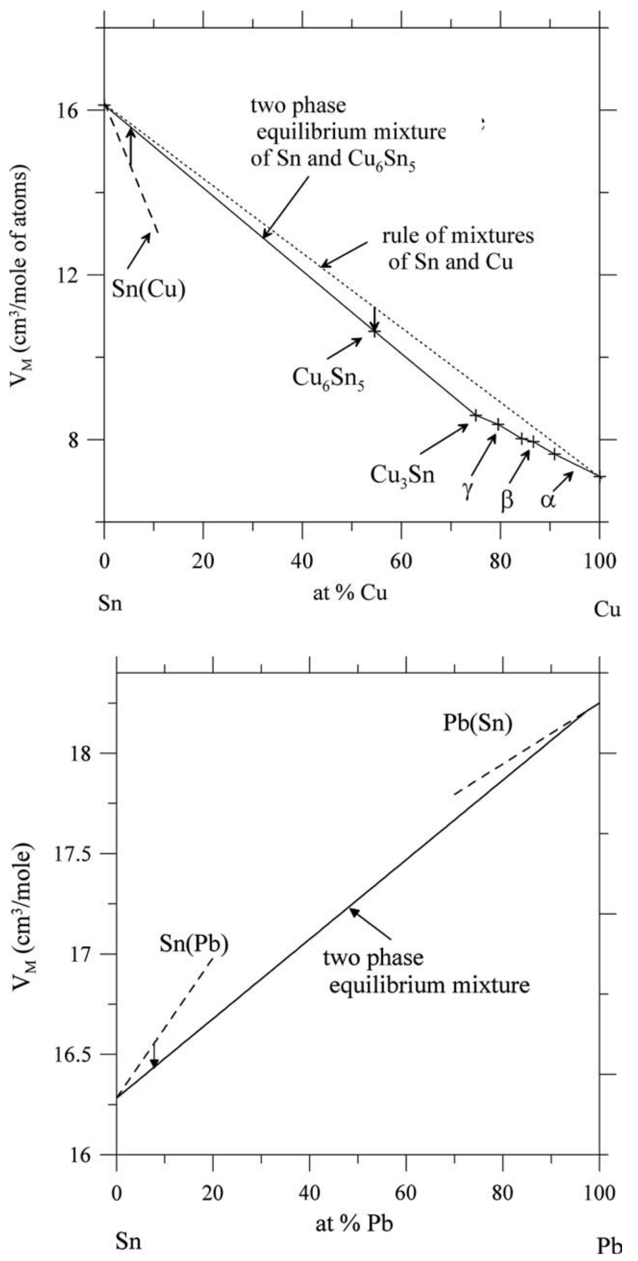

Fig. 14. Volume per mole of atoms for phases for the Sn–Cu and Sn–Pb systems. Dashed lines show supersaturated solid solutions. The vertical arrows show the volume change for the various metallurgical processes.

From Fig. 14, we can also extract the volume change when precipitation of Cu_6Sn_5 occurs from a supersaturated Sn(Cu) solid solution of mass fraction 3% Cu. It is the difference between the molar volume of the supersaturated solution and the volume of a equilibrium mixture of Sn and Cu_6Sn_5 of the same average composition

---

[2] We note that Ni also exhibits fast diffusion in Sn [35] due to its interstitial nature and would be expected to exhibit the same molar volume behavior.

as the supersaturated solution. For a deposit of 3% mass fraction Cu (5.5% atom fraction), the fractional change in volume is +0.022. That is, the volume of a supersaturated solution of Sn(Cu) expands by 2.2% when it transforms to an equilibrium mixture of Sn and Cu_6Sn_5 phases. Finally, the volume change of material that undergoes precipitation of Pb from a supersaturated Sn(Pb) solution can be obtained from the graph. For a deposit of 2% mass fraction Pb (1.16% atom fraction), the fractional change in volume is −0.0013. That is, the volume of a supersaturated solution of Sn(Pb) shrinks by 0.13% when it transforms to an equilibrium mixture of Sn and Pb phases.

5.2. Initial stress

Understanding the causes of growth stress in thin films formed by electrodeposition (and by other methods such as condensation from the vapor [36]) are active areas of research. We consider here only the difference between the stress in the pure Sn, and those in the alloy deposits. For a given thickness, we assume that the alloy deposits are formed with the same growth stress as pure Sn and that the precipitation process in the alloys shortly after deposition attempts to alter the deposit volume and hence change the stress prior to the first measurement. Table 3 gives the experimentally determined deviation of the stress-free strain values above or below that determined for the pure Sn. Also given is 1/3 of the change in the deposit volumetric strain expected from the change in molar volumes for precipitation from supersaturated solid solutions described in Section 5.1.

If the model worked perfectly, the numbers in each row of the last two columns should be the same. Similar results are obtained for the 3 and 7 μm thick electrodeposits, except the experimental increments get smaller as the thickness decreases. This explanation produces the correct trends for the alloys if not the correct numerical values; viz., that the addition of Cu increases the state of compression over pure Sn, and that Pb causes the stress to become less compressive. The quantitative errors may be due to the difficulties in measuring the deposit concentrations and/or the assumption that interstitial Cu has zero partial molar volume. A positive value would decrease the proposed amount of expansion due to Cu_6Sn_5 precipitation listed in the last column of Table 3 and improve the agreement.

5.3. Time dependence of beam deflection – average creep response

With time the precipitates coarsen, a process assumed to not alter the deposit stress. To account for the stress induced in the deposit due to the IMC formation on the interface between the deposit and the substrate requires the use of the model and equations in the Appendix. This analysis necessitates the choice of a value for the stress in the IMC layer, σ_{IMC} (more properly the stress free strain, $\varepsilon^0_{\mathrm{IMC}}$). The most negative choice for the intermetallic stress free strain is obtained using 1/3 the value of the volumetric strain for planar IMC formation from pure Sn and Cu; viz., $\varepsilon^0_{\mathrm{IMC}} = -0.02$ (see Section 5.1). Using the modulus for the IMC in Table 2, $\sigma_{\mathrm{IMC}} \approx +4.8$ GPa. This stress value is an upper bound because the IMC may not swell isotropically during growth; e.g., it might expand more in the growth direction to reduce the strain energy. A second estimate is obtained experimentally from in situ wafer curvature measurements after the deposition of 100 nm of Sn onto a Cu coated glass cantilever [16]. After 20 nm of IMC has formed, a beam deflection consistent with a tensile stress in the IMC of +1.2 GPa was obtained. A more appropriate estimate for thicker IMC layers comes from the following experiments. For three pure Sn cantilever electrodeposits, 16 μm thick and aged for approximately 3×10^7 s, the Sn was removed by dissolution in concentrated HCl. This procedure leaves the approximately 2.5 μm thick IMC behind. The deflections of the beams (compared to the original unplated position) were then +7, +30 and +37 μm; i.e., toward the deposit side. From these experiments, we conclude that σ_{IMC} is between +11 and +62 MPa ($\varepsilon^0_{\mathrm{IMC}} = -10^{-4}$ and -5×10^{-4}). Lee and Lee [11] performed similar stripping experiments but unfortunately did not report the IMC stress. Due to the uncertainty in the proper value of $\varepsilon^0_{\mathrm{IMC}}$, we will compute the stress in the electrodeposit using the deflection data and several assumed values of $\varepsilon^0_{\mathrm{IMC}}$.

Table 3
Effect of alloying addition on initial stress of 16 μm deposits

Deposit material	Measured initial stress (MPa)	Corresponding stress-free strain	Deviation of stress-free strain from that for pure Sn	1/3 of volume change due to ppt. of Cu_6Sn_5 or Pb from Cu or Pb supersaturated Sn
Sn	−15.5	2.3×10^{-4}	–	–
Sn–2%Pb	−4.0	0.6×10^{-4}	-1.7×10^{-4}	-4×10^{-4}
Sn–3%Cu	−36.5	5.6×10^{-4}	3.3×10^{-4}	7×10^{-3}

Note from the Appendix that $\varepsilon^0_{\mathrm{f}} = \varepsilon^{\mathrm{T}}_{\mathrm{f}} - \frac{\sigma_{\mathrm{f}}}{E'_{\mathrm{f}}} = -\frac{4}{3}\frac{\delta}{L^2} d_{\mathrm{S}} - \frac{\sigma_{\mathrm{f}}}{E'_{\mathrm{f}}}$.

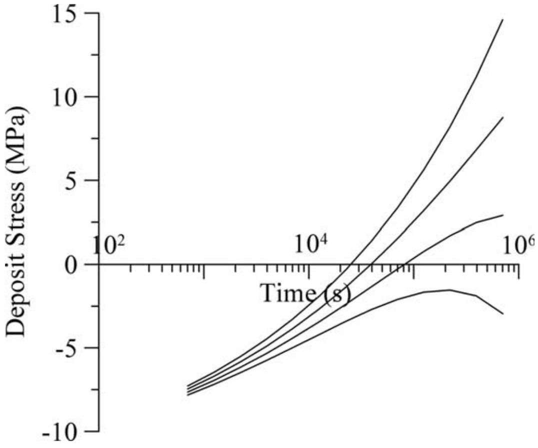

Fig. 15. Deposit stress vs. time extracted from deflection data for pure Sn, 7 μm thick samples. Curves are shown from top to bottom for four different values of the intermetallic stress-free strain, $\varepsilon^0_{\mathrm{IMC}}$: 0, -1×10^{-3}, -2×10^{-3}, -3×10^{-3}.

Using the measured deflections and the model and equations in the Appendix, we plot in Fig. 15 the deposit stress, σ_{f}, as a function of time for the 7 μm thick pure Sn deposit for several values of $\varepsilon^0_{\mathrm{IMC}}$. With $\varepsilon^0_{\mathrm{IMC}}=0$, the deposit stress changes sign from compression to tension at the same time that the beam deflection changes sign; the deflection is proportional to $\sigma_{\mathrm{f}}d_{\mathrm{f}}+\sigma_{\mathrm{IMC}}d_{\mathrm{IMC}}$, (Eqs. (A1) and (A3)). For a value $\varepsilon^0_{\mathrm{IMC}}=-3\times10^{-3}$, the stress remains compressive for all time despite the fact that the deflection changes sign. Thus, the idea presented by several authors that IMC formation on the interface between the substrate and the deposit compresses the remaining Sn is confirmed. Fig. 16 shows the different parts of the deposit strain for two of the cases shown in Fig. 15. The total deposit strain, $\varepsilon^{\mathrm{T}}_{\mathrm{f}}$, is proportional to the deflection (Eqs. (A1) and (A4)) and is positive if the deflection is negative. The relative sizes of the elastic and plastic parts derived from the model, $\varepsilon^{\mathrm{el}}_{\mathrm{f}}$ and $\varepsilon^{\mathrm{pl}}_{\mathrm{f}}$, depend on the assumed value of $\varepsilon^0_{\mathrm{IMC}}$. The elastic strain is always proportional to the stress.

The plastic strain rate is determined by differentiation of the plastic strain and a plot of log(−strain rate) vs. log(−stress) can be constructed. Such plots constitute the experimentally obtained average compression creep response of the deposits if we can assume that steady-state creep behavior applies at each instant. Reassuringly, use of a positive value of $\varepsilon^0_{\mathrm{IMC}}$ (all measurements and estimates yield negative values) leads to unrealistic plastic response; the sign of the stress and strain rate are not the same. Extremely negative values of $\varepsilon^0_{\mathrm{IMC}}$ (e.g., -2×10^{-2}) lead to equally unphysical creep curves where the stress exponent increases with decreasing compressive stress. These considerations place bounds on the value of $\varepsilon^0_{\mathrm{IMC}}$.

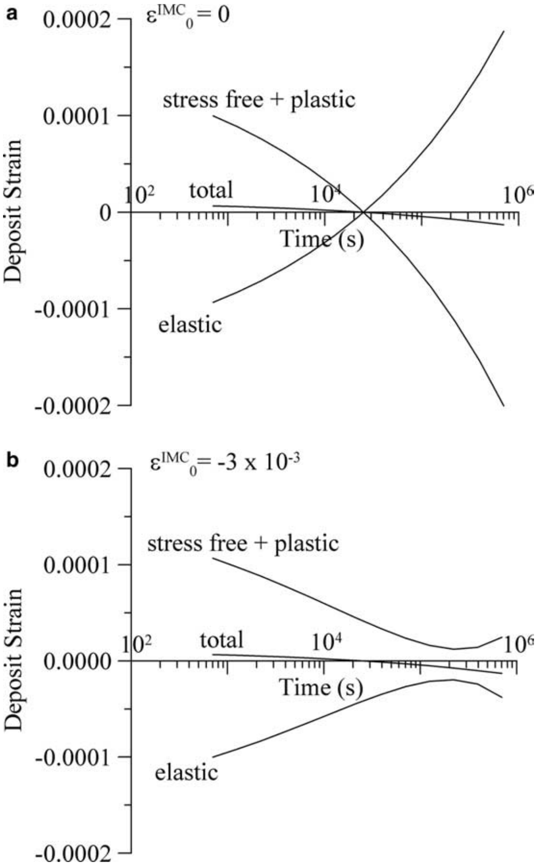

Fig. 16. Strain vs. time histories. The total deposit strain is proportional to the measured deflection. Elastic strain and stress free + plastic strain are extracted from deflection data using the model for two assumed values of intermetallic stress-free strain: (a) 0 and (b) -3×10^{-3}. Note that in (b) the elastic strain, which is proportional to the stress, is compressive for all times even though the deflection changes sign.

The creep curves for the 16 μm thick deposits are shown in Fig. 17 for three values of $\varepsilon^0_{\mathrm{IMC}}$, 0, −0.001, −0.002 that span the full range of reasonable values for the 16 μm deposits. This corresponds to IMC stress between +0 and +244 MPa. One slides down the creep curve as time progresses. For large compressive stress (early times, thin IMC), the curves are independent of $\varepsilon^0_{\mathrm{IMC}}$ and exhibit stress exponents of approximately 3, 6, and 15 for the Sn–Pb, Sn and Sn–Cu, respectively. We also note that Sn–Pb creeps faster than pure Sn, which in turn creeps faster than Sn–Cu. For smaller values of compressive stress (later time, thicker IMC), the creep curves show considerable dependence on $\varepsilon^0_{\mathrm{IMC}}$. The curves can be used to show just how much the deposit compression is increased by the intermetallic by drawing a horizontal line. Overall this analysis suggests that IMC formation on the Cu/Sn interface does not greatly increase the compressive stress over the level due to the initial plating stress in these experiments.

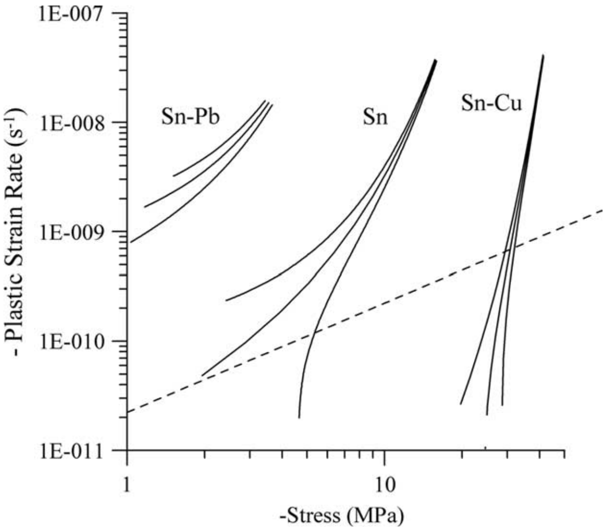

Fig. 17. log(−plastic strain rate) vs. log(−stress) for 16 μm thick electrodeposits derived from deflection measurements. For each material: bottom curve, no correction for layer intermetallic stress; center curve, corrected for layer intermetallic stress, $\varepsilon_0^{\mathrm{IMC}} = -0.001$ (stress = 125 MPa tensile); top curve, $\varepsilon_0^{\mathrm{IMC}} = -0.002$ (stress = 250 MPa tensile). The prediction of [39] for whisker growth rate (converted to average strain rate in the in-plane direction) is shown by dashed line.

5.4. Localized creep as a mechanism for whisker/hillock formation

We presume that the creep curve for Sn–Pb shown in Fig. 17 represents uniform creep alone because no whiskers, cones or hillocks form. The electrodeposit would swell slightly and uniformly in thickness as the compressive stress relaxes. For incompressible plasticity, the plastic strain (strain rate) normal to the electrodeposit surface equals minus two times the in-plane strain (strain rate). On the other hand, the creep curves for Sn and Sn–Cu include the non-uniform creep that produces the surface disruption. In other words the hillock and whisker formation is part (or all) of the compression creep response of these materials when constrained by a substrate. We note that the creep rates of the pure Sn and Sn–Pb deposits are much slower than those reported for bulk samples of similar compositions with the same grain size [37,38].

As mentioned in Section 1, diffusional creep has been employed to explain hillock growth in thin films. Following this approach, Tu [10] and Hutchinson et al. [39] have proposed models for whisker growth velocity based on an imposed constant in-plane compressive stress and grain boundary diffusion of Sn to the whisker base. Grain boundary diffusion is expected to be the dominant self diffusion mechanism in Sn because the homologous temperature for Sn corresponding to room temperature is 0.6. With whiskers a distance $2b$ apart and with diameter $2a$, both models arrive at a tip growth velocity v given by

$$v = -\ell\left[\frac{2D_{\mathrm{gb}}\Omega}{RTa^2\ln(b/a)}\right]\sigma_{\mathrm{f}}, \qquad (7)$$

where Ω is the molar volume of Sn, D_{gb} a grain boundary diffusion coefficient, RT is the Boltzmann factor and a signed stress, σ_{f}, has been used. A stress gradient in the deposit with cylindrical symmetry under each whisker is assumed to drive the flux of Sn toward that whisker. The length differs in the two models significantly depending on the geometrical details. The model of Hutchinson et al., which uses 2 $\ell D_{\mathrm{gb}}/g$, the deposit thickness, and replaces D_{gb} with $D_{\mathrm{gb}}\frac{2\lambda}{g}$, where λ and g are the effective thickness of a grain boundary and the grain size, respectively, leads to the correct order of magnitude of whisker growth rate using the literature accepted values of the Sn grain boundary diffusion coefficient [40]. From these models, one can compute the plastic strain rate normal to the deposit if it were averaged over the entire deposit

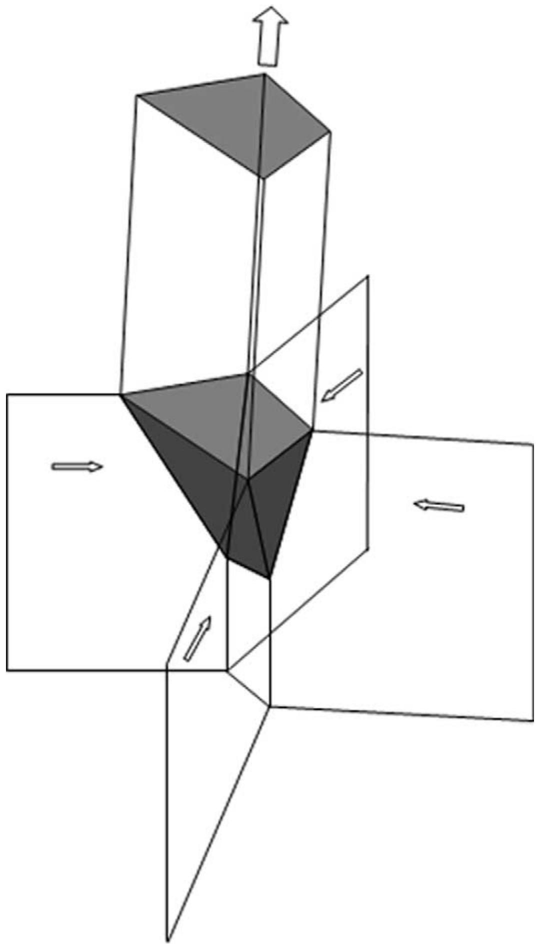

Fig. 18. Region of a deposit near its surface that contains a small grain with interior oblique faces surrounded by columnar grains under biaxial compressive stress. The three-dimensional path of Sn atoms to relieve the stress is along columnar grain faces (arrows) within the deposit, through the triple lines, and across the oblique (black) faces. Accretion of Sn on these faces forces the whisker above the deposit surface.

surface as va^2/b^2d_f; giving an in-plane creep rate for an incompressible deposit of $-va^2/2b^2d_f$ or

$$\dot{\varepsilon}_f = \frac{\ell}{d_f}\frac{\Omega D_{gb}}{RTb^2\ln(\frac{b}{a})}\sigma_f. \tag{8}$$

We note that this prediction is linear in stress and would produce a creep rate with slope of unity as superimposed in Fig. 17, where we have used $\ell = d_f$, $\lambda D_{gb} = 6\times10^{-22}$ m^3/s [40], $g = 3\ \mu m$, $\Omega = 1.7\times10^{-5}\ m^3/mol$, $a = 2\ \mu m$ and $b = 100\ \mu m$.

It is interesting to note, despite the approximations of this whisker growth model, that the average strain rate derived from this model is roughly tangential to the creep curves for the pure Sn, lies below the creep curves for Sn–Pb and cuts through the creep curve for Sn–Cu. As a mechanism of creep, whisker growth would then be least active for Sn–Pb, be marginal for pure Sn and occur readily for Sn–Cu. For Sn–Cu, creep likely occurs by a mechanism with high exponent before whisker creep becomes dominant at lower compressive stress. This may be related to the observation that whisker formation appears to have an "incubation time".

The above calculation for whisker growth rate needs improvement. A detailed model is beyond the scope of the present paper, but it would be a special case of Coble creep [41]. The diffusion potential (chemical potential of Sn atoms minus chemical potential of vacancies) is highest for grain faces with the most compressive normal stress. This would correspond to grain faces with normals lying in the plane of the deposit due to the bi-axial in-plane stress state; i.e., the columnar grain faces. Oblique grain faces would have lower diffusion potential and grain faces parallel to the deposit surface would be least. (The surface of the deposit would also have the least diffusion potential, but we presume surface diffusion is suppressed by native oxide.) This difference in diffusion potential causes a flux of Sn along the normal grain faces to oblique faces. If many oblique or parallel faces are located within the deposit (as with the Sn–Pb deposits), creep is relatively uniform and no hillocks/whiskers would occur. Averaged over many grains this uniform creep process leads to a slight thickening of the deposit and a reduction in the in-plane stress without whisker formation.

If oblique or parallel faces occur rarely, as in the columnar structures of the Sn and Sn–Cu samples, the diffusion flux is forced toward the free surface. Any oblique grain face near, but under, the deposit surface

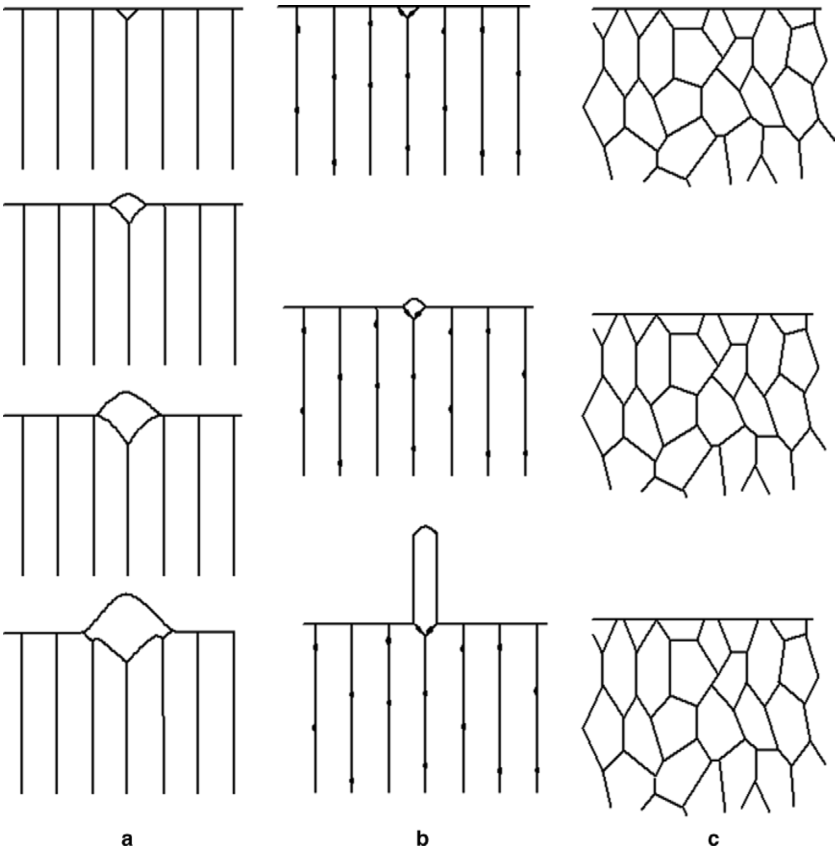

Fig. 19. Due to the absence of transverse grain boundaries in the columnar grain structures of (a) Sn or (b) Sn–Cu, in-plane compressive stress is relieved by hillock or whisker growth, respectively, depending on whether the grain boundaries are (a) mobile or (b) pinned. In the more equi-axed structure of Sn–Pb, uniform creep is possible and there is no need to form surface protrusions.

would be ripe for accumulation of Sn and pushing of the grain upward to produce surface features, such as hillocks and whiskers. As with any diffusional creep process, grain boundary sliding and accommodation must occur simultaneously [42]. We note however that Sheng et al. [22] observe whisker growth from matte Sn and Sn–Cu deposits even though the grain structure is not columnar. Thus, avoiding columnar grain structures should be considered only part of a general whisker mitigation strategy.

A proper model for whisker growth from a columnar grain structure must assess the grain boundary diffusion path through a three-dimensional network of columnar grain faces connecting to oblique grain faces near the deposit surface, for example at a small surface grain as shown in Fig. 18. Whisker growth would only be possible at a few small surface grains formed at the end of the deposition process or possibly by recrystallization after plating. Fig. 19 shows different situations for the response of a small surface grain depending on the general grain shape and mobility of the grain boundaries in the electrodeposits. Fig. 19(a) shows the case for pure Sn deposits with a columnar grain structure in which the active surface grain can broaden laterally by grain boundary migration as it is pushed upward. The localized creep is thus spread over a larger surface area; never forming a filamentary whisker. In a film under stress, the seeds of a model for this lateral grain boundary motion and surface upheaval on the trailing side can be found in [43]. Many hillocks appear to have a small flat top at their center indicating the original location of the hillock grain prior to the migration of its boundaries. For very thin deposits, hillock base broadening may be halted when the hillock grain bottom has impinged on the layer IMC. If sufficient compressive stress remains, the hillock may then grow in a more whisker-like manner. Such a process may be important for deposits with thickness the same as the lateral grain size.

In Fig. 19(b) is depicted the situation for the Sn–Cu deposits where the grain boundaries are pinned or impeded by IMC particles. These particles are formed by precipitation from Sn supersaturated solid solution formed by co-deposition of Sn and Cu from the electrolyte. Hillock grain base broadening is hindered and the upward motion of material is concentrated into contorted hillocks or whiskers. Contorted hillocks occur when several surface grains with oblique internal faces in close proximity are present; hence, the multi-grained nature seen in Fig. 6. Whiskers occur when a single surface grain with immobile oblique internal faces persists in time for the Sn flux to continually accrete. Fig. 19(c) shows the case of the non-columnar structure of Sn–Pb where many internal grain boundaries are available for accretion of Sn producing a more uniform thickening of the deposit to relieve compressive stress.

6. Conclusions

1. Plating on cantilever beam samples shows that compressive stresses are present in high purity bright Sn electrodeposits within 15 min after plating. Intermetallic growth along the Sn/Cu interface should be insignificant (6 nm thickness) over this short time at room temperature. Thus, compressive stresses are intrinsic to the plating process under the conditions of our experiments.
2. Co-deposition of Sn with Cu or Sn with Pb in the amount of a few mass percent alters the compressive stress compared to pure Sn by the time of first measurement. Larger compressive stress is generated in the electrodeposit with Cu addition to the electrolyte; smaller compressive stress is generated in the deposit with Pb addition to the electrolyte. The increase/decrease in compressive stress for the alloys is due to volume changes of the deposit caused by the solid state precipitation of Cu_6Sn_5/Pb particles by metallurgical precipitation from the supersaturated Sn–Cu/Sn–Pb solid solution formed by the plating process.
3. Cu addition does not alter the columnar grain structure found in pure Sn deposits, whereas the Pb addition causes an equi-axed grain structure to develop.
4. The analysis of the time dependence of the measured beam deflections indicates that the additional compressive stress due to intermetallic formation on the deposit/beam interface over long time periods is of the same order of magnitude as the plating stress. It is not the sole source of compressive stress.
5. Whiskers and contorted hillocks are observed on the Sn–Cu deposit surfaces, conical hillocks are observed on the pure Sn deposits and no surface disturbances are found on the Sn–Pb deposits.
6. We propose that the compressive stress in the deposits relaxes by Coble creep (grain boundary transport of Sn and vacancies). For the equi-axed structure of the Sn–Pb deposits, transport between interior grain faces with different normal stress permits uniform swelling of the deposit thickness and no localized surface disturbance. For the columnar structures of the Sn and Sn–Cu deposits, the Sn flows toward the free surface. In the absence of surface transport due to native oxide, the Sn accumulation is localized to oblique grain faces near but under the free surface that forces the grain upward.
7. The lack of lateral grain boundary mobility of the columnar structure in the Sn–Cu deposits caused by precipitate pinning is thought to promote whisker formation by maintaining a laterally small grain where Sn flux accumulates. Rather benign (electronically) hillock formation occurs in pure Sn due to extensive lateral grain boundary migration.

8. A suggested whisker mitigation strategy based on this work would be to avoid impurities in the electrolyte such as Cu that are fast diffusers and hence occupy interstitial sites in the Sn lattice. Electrolytes containing solutes occupying substitutional sites in the Sn lattice and also whose precipitation from supersaturated solid solution tends to reduce the volume of the deposit should be beneficial.
9. A second suggestion is to employ plating conditions and/or additives to the electrolyte that break up the columnar structure and promote the formation of grain boundaries parallel to the deposit surface. Such boundaries would allow a more uniform creep of electrodeposits to relieve compressive stress.

Acknowledgments

The authors are indebted to R. Parke and S. Claggett for the TEM sample preparation, to R. Fields for the phosphor bronze mechanical measurements, U.R. Kattner for thermodynamic calculations and to Daniel Josell for many fruitful discussions regarding beam deflection. Thanks are also in order to G. Galyon and M. Palmer for the FIB pictures, which greatly clarified the microstructures and assisted this research.

Appendix. Time-dependent deflection of a beam with two thin films

To estimate the stresses in each layer, which cannot be individually determined from the beam deflection, we develop a model to describe the time-dependent deflection of the beam. The deflection is due to three causes: (1) an initial residual stress in the deposit due to plating and fast precipitation processes, that is assumed independent of time; (2) stress due to the growth of a layer of IMC that forms between the Sn and Cu substrate that has a different volume than the Sn and Cu from which it formed; (3) relaxation due to creep. The model assumes that the creep is uniform. For this model, we will employ the thin deposit approximation, to avoid unnecessary complication in the exposition.

Let σ_i, d_i, ε_i, E'_i be the stress, thickness, strain and modulus in layer i, where i = IMC or f for the planar IMC layer and electrodeposited film, respectively. Let the beam curvature be given by

$$K(t) = \frac{1}{r(t)} = \frac{2\delta(t)}{L^2}, \tag{A1}$$

where $\delta(t) > 0$ if the electrodeposit surface is concave (deposit on top, curved up). To treat the fact that the IMC layer thickens with time and the Sn layer thins with time, we use:

$$\begin{aligned} d_{\mathrm{IMC}}(t) &= \sqrt{Bt}, \\ d_{\mathrm{f}} &= d_{\mathrm{f}}^0 - s d_{\mathrm{IMC}}(t), \\ d_{\mathrm{S}} &= d_{\mathrm{S}}^0 - (1-s) d_{\mathrm{IMC}}, \end{aligned} \tag{A2}$$

where $s \approx 5/11$. For d_{IMC} and $d_{\mathrm{f}} \ll d_{\mathrm{S}}$, balance of moments and forces for the substrate and the two layers yields

$$\sigma_{\mathrm{IMC}}(t) d_{\mathrm{IMC}}(t) + \sigma_{\mathrm{f}}(t) d_{\mathrm{f}}(t) = \frac{E'_{\mathrm{S}}}{6} (d_{\mathrm{S}}(t))^2 K(t). \tag{A3}$$

With the thin approximation, the total strain in both layers (measured from a flat beam) is the same and is given by

$$\varepsilon_{\mathrm{IMC}}^{\mathrm{T}} = \varepsilon_{\mathrm{f}}^{\mathrm{T}} = -\frac{2}{3} d_{\mathrm{S}}(t) K(t). \tag{A4}$$

The total strain in the IMC layer will be assumed to be the sum the stress-free strain due to its volume change from the reactants and its stress-dependent elastic strain (no creep)

$$\varepsilon_{\mathrm{IMC}}^{\mathrm{T}} = \varepsilon_{\mathrm{IMC}}^{0} + \varepsilon_{\mathrm{IMC}}^{\mathrm{el}} \tag{A5}$$

with

$$\sigma_{\mathrm{IMC}} = E'_{\mathrm{IMC}} \varepsilon_{\mathrm{IMC}}^{\mathrm{el}} = E'_{\mathrm{IMC}} [\varepsilon_{\mathrm{IMC}}^{\mathrm{T}} - \varepsilon_{\mathrm{IMC}}^{0}]. \tag{A6}$$

The total strain in the Sn deposit will be assumed to be the sum of the stress free strain due to the electrodeposition process (plus the fast precipitation processes in the alloys), stress-dependent elastic and plastic strains

$$\varepsilon_{\mathrm{f}}^{\mathrm{T}} = \varepsilon_{\mathrm{f}}^{0} + \varepsilon_{\mathrm{f}}^{\mathrm{el}} + \varepsilon_{\mathrm{f}}^{\mathrm{pl}} \tag{A7}$$

with

$$\sigma_{\mathrm{f}} = E'_{\mathrm{f}} \varepsilon_{\mathrm{f}}^{\mathrm{el}} = E'_{\mathrm{f}} [\varepsilon_{\mathrm{f}}^{\mathrm{T}} - \varepsilon_{\mathrm{f}}^{0} - \varepsilon_{\mathrm{f}}^{\mathrm{pl}}] \tag{A8}$$

and

$$\dot{\varepsilon}_{\mathrm{f}}^{\mathrm{pl}} = f(\sigma_{\mathrm{f}}), \tag{A9}$$

where the dot denotes a time derivative. The function $f(\sigma_{\mathrm{f}})$ could represent power law creep for example of the form

$$\dot{\varepsilon}_{\mathrm{f}}^{\mathrm{pl}} = K \sigma_{\mathrm{f}}^{n}. \tag{A10}$$

For choices of a parabolic growth constant B, and a value for $\varepsilon_{\mathrm{IMC}}^{0}$, one can extract $\sigma_{\mathrm{f}}(t)$ and the quantity $[\varepsilon_{\mathrm{f}}^{0} + \varepsilon_{\mathrm{f}}^{\mathrm{pl}}(t)]$ or its time derivative $\dot{\varepsilon}_{\mathrm{f}}^{\mathrm{pl}}(t)$ from the measured data, $\delta(t)$. On can then plot log strain rate vs. log stress for the electrodeposit to estimate the function, Eq. (A9). Because the stress and strain rates are negative (compression creep), absolute values are used for Fig. 17.

Alternately, one can convert these equations to a system of coupled ordinary differential equations for $\delta(t)$, $\sigma_{\mathrm{f}}(t)$, $\sigma_{\mathrm{IMC}}(t)$ and $\varepsilon_{\mathrm{f}}^{\mathrm{pl}}(t)$ for a given creep law and the other materials parameters. Numerical solution shows how the electrodeposit stress is affected by the growing IMC. In general, the stress in the film becomes slightly more compressive due to the IMC growth. The amount is sensitive to the how positive is the chosen value of $\varepsilon^0_{\mathrm{IMC}}$.

References

[1] Furuta N, Hamamura K. Jpn J Appl Phys 1969;8:1404.
[2] Chason E, Kabakian L, Kumar S. Materials for space applications. In: Chipara M, Edwards DL, Benson RS, Phillips S, editors. Mater Res Soc Symp Proc, vol. 851, Warrendale, PA; 2005. p. NN5.17.
[3] Fisher RM, Darken LS, Carroll KG. Acta Metall 1954;2:368.
[4] Arnold SM. Plating 1966;53:96.
[5] Galyon GT. Annotated Tin Whisker Bibliography, National Electronics Manufacturing Initiative Inc. (NEMI), Herdon, VA, July; 2003. Available from: www.nemi.org.
[6] Chadhari P. J Appl Phys 1974;45:4339.
[7] Jackson MS, Li C-Y. Acta Metall 1982;30:1993.
[8] Doerner MF, Nix WD. CRC Crit Rev Solid State Mater Sci 1988;14:225.
[9] Tu KN. Acta Metall 1973;21:347.
[10] Tu KN. Phys Rev B-Cond Matter 1994;49:2030.
[11] Lee BZ, Lee DN. Acta Mater 1998;46:3701.
[12] Moon K-W, Williams ME, Johnson CE, Stafford GR, Handwerker CA, Boettinger WJ. In: Hanada S, Zhong Z, Nam SW, Wright RN, editors. Proceedings of the fourth pacific rim international conference on advanced materials and processing. Sendai, Japan: The Japanese Institute of Metals; 2001. p. 1115–8.
[13] Weil R. Plating 1971;58:137.
[14] Onishi M, Fujibuchi H. Trans J Inst Metal 1975;16:539.
[15] Tu KN, Thompson RD. Acta Metall 1982;30:947.
[16] Stafford GR, Bertocci U, Guyer JE, NIST; 2004 [unpublished research].
[17] Bard AJ, Faulkner LR. Electrochemical methods: fundamentals and applications. New York, NY: Wiley; 1980. p. 288.
[18] Galyon GT, Palmer M, IBM; 2004, unpublished images of NIST samples.
[19] Petersson I, Ahlberg E. J Electroanal Chem 2000;485:166.
[20] Tindall GW, Bruckenstein S. Anal Chem 1968;40:1402.
[21] Brenner A. Electrodeposition of alloys, vol. 1. New York, NY: Academic Press; 1963. p. 195.
[22] Sheng GTT, Hu CF, Choi WJ, Tu KN, Bong YY, Nguyen L. J Appl Phys 2002;92:64.
[23] Kane RH, Giessen BC, Grant NJ. Acta Metall 1966;14:605.
[24] Kim D-K, Nix WD, Deal MD, Plummer JD. J Mater Res 2000;15:1709.
[25] Brenner A, Senderoff S. J Res NBS 1949;42:105.
[26] Smithells CJ. Metal reference book. 4th ed. New York, NY: Plenum Press; 1967.
[27] Fields RJ, Low III SR, Lucey Jr GK. In: Cieslak MJ, Perepezko JH, Kang S, Glicksman ME, editors. Metal science of joining. Warrendale, PA: The Minerals, Metals & Materials Society; 1992. p. 165–73.
[28] Saunders N, Miodownik AP. Bull Alloy Phase Diagram 1990;11:278.
[29] Homer CE, Plummer H. J Inst Metal 1939;64:169.
[30] Kattner UR. NIST, Gaithersburg, MD; 2002 [unpublished research].
[31] Dyson BF, Anthony TR, Turnbull D. J Appl Phys 1967;38:3408.
[32] Warburton WK, Turnbull D. Thin Solid Films 1975;25:71.
[33] Karakaya I, Thompson WT. Bull Alloy Phase Diagram 1988;9:144.
[34] Lee JA, Raynor GV. Proc Phys Soc 1954;67:737.
[35] Yeh DC, Huntington HB. Phys Rev Lett 1984;53:1469.
[36] Floro JA, Chason E, Cammarata RC, Srolovitz D. MRS Bull 2002;27:19.
[37] Schneibel JH, Hazeldine PM. J Mater Sci 1983;18:562.
[38] McCabe RJ, Fine ME. Metall Mater Trans 2002;33A:1531.
[39] Hutchinson B, Oliver J, Nylén M, Hagström J. Mater Sci Forum 2004;467–470:465.
[40] Kaur I, Gust W. Handbook of grain boundary and interface boundary diffusion data, vol. 2. Stuttgart: Ziegler Press; 1989. p. 1277.
[41] Coble RL. J Appl Phys 1963;34:1679.
[42] Raj R, Ashby MF. Metall Trans 1971;2:1113.
[43] Genin FY. J Appl Phys 1995;77:5130.